Materials and Design 153 (2018) 221–231

Contents lists available at ScienceDirect

Materials and Design

journal homepage: www.elsevier.com/locate/matdes

Incipient plasticity and surface damage in $LiTaO_3$ and $LiNbO_3$ single crystals

M. Gruber [a], A. Leitner [b], D. Kiener [b], P. Supancic [a], R. Bermejo [a,*]

[a] Institut fuer Struktur- und Funktionskeramik, Montanuniversitaet Leoben, Peter-Tunner-Strasse 5, A-8700 Leoben, Austria
[b] Department Materials Physics, Montanuniversitaet Leoben, Jahnstraße 12, A-8700 Leoben, Austria

GRAPHICAL ABSTRACT

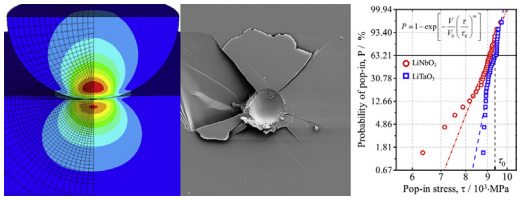

ARTICLE INFO

Article history:
Received 12 January 2018
Received in revised form 19 April 2018
Accepted 30 April 2018
Available online 03 May 2018

Keywords:
Nanoindentation
Single crystals
Anisotropy
Pop-in
Twinning
Cracking

ABSTRACT

The outstanding functional properties of single crystals used in many engineering applications often rely on their surface quality. The associated grinding process in single crystals is known to introduce surface or sub-surface defects (cracks), which may compromise the functionality and/or structural integrity of the final device. The small size of such defects often yields relatively high strength values, but also usually large scatter which implies low reliability. The aim of this work is to analyze the onset of surface contact damage in single crystals with respect to crystal orientation and elastic properties. $LiTaO_3$ and $LiNbO_3$ anisotropic single crystal samples are investigated using nanoindentation techniques and focused ion beam based sub-surface analyses. Experimental findings show that the onset of damage is correlated to weaker cleavage planes. At this stage also traces of plastic deformation on the contact surface due to twinning are observed. Further load increase revealed contact cracks in both materials; their morphology and extension being related to the orientation of the cleavage planes and elastic properties of the crystals. Our results advance the understanding of damage in anisotropic materials such as $LiTaO_3$ and $LiNbO_3$, and can generally be utilized to assess the onset of damage in other brittle materials.

1. Introduction

The use of single crystals in engineering applications has been motivated by their outstanding optical, electrical and mechanical properties. A first example is the use of single crystals as gain media for solid state lasers. Particular single crystals also show high dielectric (or piezo-electric) response, which is of prime interest for sensors and actuators. Another example is silicon, which is indispensable in modern semiconductor-based microelectronic components. Special attention has been drawn to single crystal materials for communication technologies; in particular the use of piezoelectric materials as surface acoustic wave frequency filters [1]. Here the piezoelectricity is used for converting electrical frequencies into mechanical, acoustic waves, which are then filtered by destructive/constructive interferences and converted back into electrical output signals, exhibiting the desired bandpass characteristics. Two candidate materials for acoustic filter applications are Lithium Tantalate ($LiTaO_3$) and Lithium Niobate ($LiNbO_3$), as they exhibit particular low acoustic losses [2–4]. Despite their unique properties, brittle single crystals are in general limited in most applications because they lack the

* Corresponding author.
E-mail addresses: manuel.gruber@unileoben.ac.at, (M. Gruber), alexander.leitner@unileoben.ac.at, (A. Leitner), daniel.kiener@unileoben.ac.at, (D. Kiener), peter.supancic@unileoben.ac.at, (P. Supancic), raul.bermejo@unileoben.ac.at (R. Bermejo).

https://doi.org/10.1016/j.matdes.2018.04.082
0264-1275/

structural integrity of (for instance) polycrystalline ceramics. Also for piezoelectronic applications the mechanical properties are topics of recent research [5–7]. Single crystals often show a high anisotropy in their macroscopic physical properties (e.g. coefficient of thermal expansion, elastic modulus), giving rise to significantly different functional properties along individual crystallographic directions. From the application point of view, the mechanical response of single crystals is associated with the orientation of cleavage planes, twinning planes or slip planes with respect to the applied load. The resistance of brittle single crystals to fracture (its fracture toughness) is generally low, on the order of ~$1 \cdot MPam^{1/2}$ [8]. Therefore, the propagation of existing (microstructural) defects upon loading yields brittle fracture, thus compromising the functionality of the component for which the single crystalline material has been designed. The strength limiting factors in brittle single crystals are usually pre-existing flaws coming from the harsh cutting, grinding or polishing processes, as well as sub-surface cracks which are a result of contact loading during assembly procedures [9–12]. For the particular application as surface acoustic wave filters, further damage during pick and place of the microelectronic device may occur due to high contact pressures coming from the small contact area between needle and single crystal material. Depending on the damaged area below the loaded region of a brittle material, gradual or abrupt losses in strength are documented and associated with quasi-plastic damage or cone cracking, respectively [13–16]. The small size of such defects often yields relatively high characteristic strength values, but usually large scatter (low reliability) due to the broad defect size (and orientation) distribution [17,18]. It is thus mandatory to characterize the mechanical response of single crystals, with special attention to the orientation of the crystal with respect to the loading direction. In this regard, only few works are found in literature concerning the response of $LiTaO_3$ or $LiNbO_3$ to mechanical loading, mainly restricted to loading along [0001] or [01$\bar{1}$0] directions [19–23]. However, different orientations are used for engineering devices [4,24], which can exhibit different mechanical response due to the anisotropic material properties in single crystals and deformation mechanisms acting on a particular high stressed crystal plane. Both, cracks as well as plastic deformation, can influence the functionality (e.g. piezo or damping properties due to different domain structures [25]) of certain materials.

Previous mechanical characterization of these two materials revealed a significant difference in the biaxial strength of wafer samples, with characteristic strengths of ~700 MPa for $LiNbO_3$ versus ~1800 MPa for $LiTaO_3$ [18]. Corresponding fractographic (post-mortem) analyses revealed different sub-surface damage between both materials (i.e. deeper scratches in $LiNbO_3$). However, an understanding of the damage process during loading is still lacking. The aim of this work is to assess the onset of damage in single crystals by combining nanoindentation techniques with focus ion beam (FIB) analyses. The reference materials used for this study are $LiTaO_3$ and $LiNbO_3$, having different orientations with respect to their growth direction. Nanoindents were performed using a Berkovich and a spherical indenter tip at incremental loads to retrieve the elastic properties of the single crystals and capture the onset of plastic deformation and damage. Results are interpreted in the framework of contact mechanics and Weibull statistics, and the conclusions drawn can be extended to other brittle or quasi-brittle materials.

2. Material of study, sample orientation and used methods

$LiNbO_3$ and $LiTaO_3$ are trigonal crystals belonging (below the Curie temperature) to the 3 m point group and the *R*3*c* space group (no. 161), usually represented using hexagonal axes ($a = b \neq c$ and $\alpha = \beta = 90°, \gamma = 120°$) [26,27]. Both crystals show threefold rotation symmetry around the c_h – axis which exhibits the strongest atomic bonds, leading to the highest Young's modulus and lowest coefficient of thermal expansion in this direction [28,29]. To enhance the functionality in terms of e.g. high wave velocities, large electromechanical coupling factors, low temperature dependencies of delay and center frequency together with low insertion/propagation losses, a particular orientation depending on the further application is usually pursued for each material. In this context, an optimized wafer for the application as SAW-filter substrate is provided in Fig. 1, where the [0001] direction is rotated 48° counterclockwise for $LiTaO_3$ (Fig. 1a) and 38° clockwise for $LiNbO_3$ (Fig. 1b) around the [2$\bar{1}\bar{1}$0] axis, marked with the wafer flat. This leads to an angle between the wafer's surface and the [0001] direction of 42° and 128° for $LiTaO_3$ and $LiNbO_3$, respectively. The two materials are therefore referred to as 42° Y-X $LiTaO_3$ and 128° Y-X $LiNbO_3$, where the latter one is already known since 1976 for its extraordinarily high electromechanical coupling coefficient and wave velocity [24]. The corresponding alignment of low indexed planes is provided in the pole figures for $LiTaO_3$ (Fig. 1c) and for $LiNbO_3$ (Fig. 1d), with dimensions of the unit cells taken from Hsu et al. [30]. Relevant planes for the deformation and damage analysis in this work are highlighted with larger colored dots. It is worth pointing out that while for 128° Y-X $LiNbO_3$ the (0$\bar{1}$14) plane is parallel to the surface (in the center of Fig. 1d), no low indexed plane corresponds to the wafer surface of the 42° Y-X $LiTaO_3$. The (01$\bar{1}$2) plane is, with an inclination angle of 9°, relatively parallel to the surface (close to the center in Fig. 1c).

Samples with the respective orientation were diced and ground by the company EPCOS OHG, Deutschlandsberg, Austria (a TDK group company). A mirror-polished surface was provided. Nanoindentation experiments were performed on these $LiNbO_3$ and $LiTaO_3$ specimens to determine hardness, indentation equivalent elastic modulus and onset of damage in both single crystalline materials. The Indentation tests were made at room temperature using a G200 nanoindenter (Keysight-Tec, Santa Rosa, California, USA) equipped with a continuous stiffness measurement (CSM) unit. Two diamond tips with (i) a Berkovich and (ii) a spherical geometry with a radius of 4.5 μm (Synton-MDP AG, Nidau, Switzerland) were used and calibrated on fused silica. Note that the spherical character of the latter is featured only up to 1300 nm, where the conical base with a total opening angle of 90° intersects the sphere. Since this occurs well beyond the point of pop-in and the used area function of the tip can describe the entire mixed geometry, this will not affect any presented results. Displacement controlled experiments were executed with constant strain rates ($\dot{P}/P = 0.05\ s^{-1}$) for Berkovich measurements. The displacement amplitude of the CSM signal was set to 2 nm oscillating at a frequency of 45 Hz to overcome influences of the integrated lock-in amplifier [31]. Thermal drift was measured in a post-test segment and did not exceed 0.3 nm/s for any considered indent. Hardness and indentation equivalent elastic modulus were evaluated according to the classical analysis for isotropic samples of Oliver and Pharr [32]. As proposed by Vlassak and Nix, for anisotropic materials a correction of this value can be employed [33,34]. Since the anisotropy factor of $LiTaO_3$ as well as $LiNbO_3$ is low (1.3 and 1.4, respectively, calculated using data from [29]), the maximum possible error is expected within 2% [33,34]. Thus, this correction is within the measurement uncertainties and was neglected for the sake of simplicity. Tip calibration, especially of spherical indenters, must be carefully performed to account for well-known tip shape imperfections. For this purpose, in an analogue procedure to the conventional Oliver-Pharr method for pyramidal shapes [32], the used tips were calibrated on elastic isotropic fused quartz. However, the function type used to describe the projected area in dependence of the displacement must be modified for spherical indenters. In a previous study it was demonstrated that a three-parameter function, based on the geometry of a perfect sphere, is well suited to describe tips which feature a rather ellipsoid shape. Further details are given in reference [35].

The required onset of first irreversible damage might slightly depend on the apparent strain-rate as well as the stressed volume [36–38],

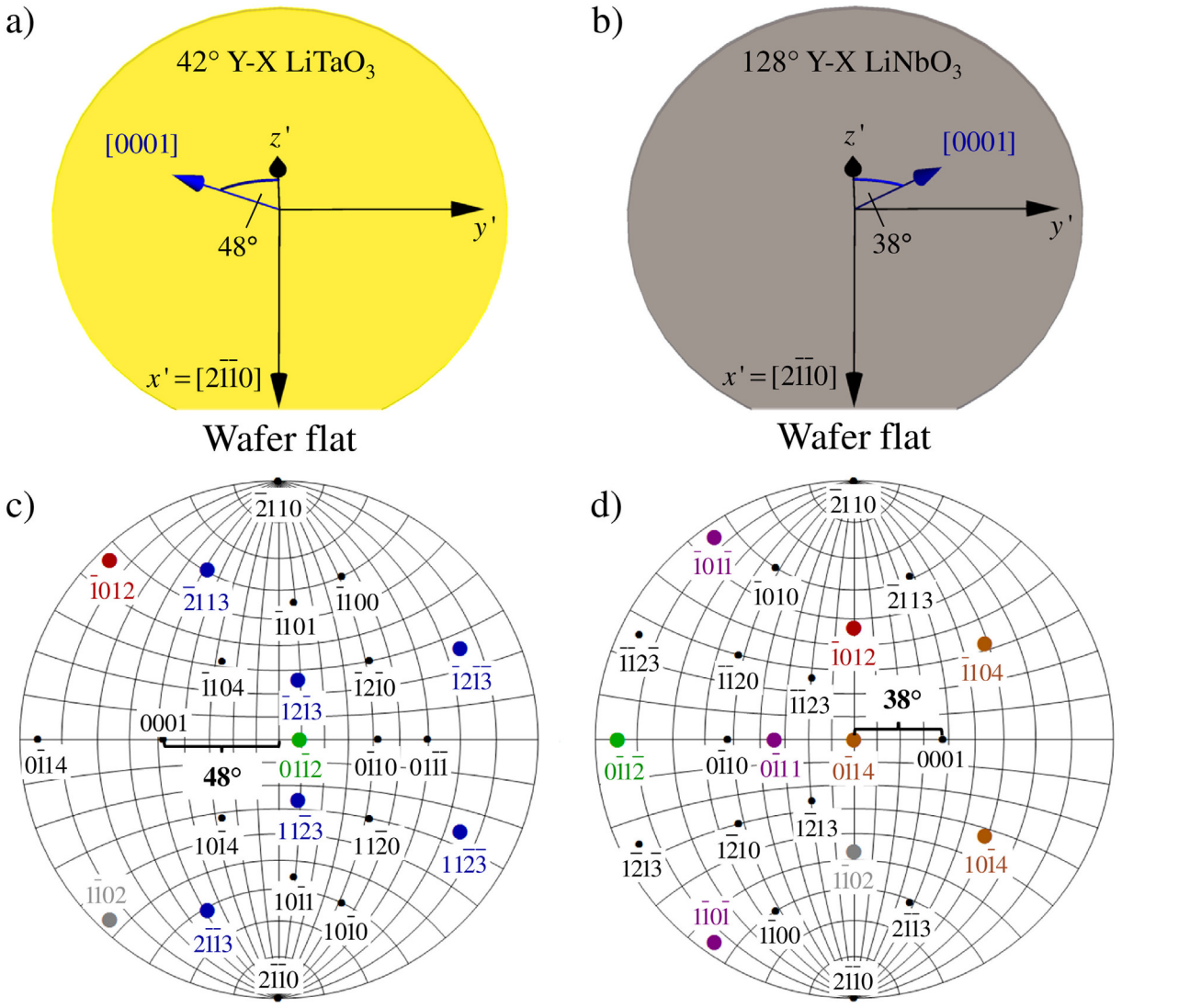

Fig. 1. Crystallographic orientation of the used wafers for $LiTaO_3$ (a) and $LiNbO_3$ (b) with corresponding pole figures (grid size of 10 × 10°) containing low indexed crystallographic planes (full symbols). Planes contributing to the observed deformation/damage of the materials are highlighted with larger (colored) dots.

which in turn correlates with the used tip radius. Due to the fact that the recorded elastic modulus over displacement shows a constant value for the investigated materials, an elastic anisotropy effect due to a changing strain - or stress-field, which also comes along with a changing tip radius, is not expected. On the other hand, the effective tested volume of the deformation zone would significantly increase for larger radii, hence it is likely that lower hardness values and pop-in stresses may be obtained due to the increasing probability of encountering pre-existing defects in larger volumes. However, using the same experimental indentation parameters for the two similar materials clearly guarantees an eligible qualitative comparison between $LiNbO_3$ and $LiTaO_3$, even though only one tip radius was employed. All specimens were loaded parallel to the z′ direction shown in Fig. 1a and b.

Surface images were made using a Scanning Electron Microscope (SEM, Zeiss LEO 1525, Oberkochen, Germany) with an acceleration voltage of 10 kV and a beam-current of 200 nA. Focused Ion Beam (FIB) cross-sections of the indented material were prepared using a FIB working station (Auriga, Zeiss, Oberkochen, Germany) equipped with a gallium FIB system (Cobra Z-05, Orsay Physics, Brno, Czech Republic), operated at 30 kV. Coarse cuts were performed with a high current Ga-beam of 20 nA and systematically reduced down to 100 pA for the final surface polishing step.

3. Results and discussion

3.1. Material response to Berkovich nanoindentation tests

Fig. 2 shows the load (P) versus displacement (h) curves of both $LiTaO_3$ and $LiNbO_3$ single crystalline samples using a Berkovich tip. The curves with steeper slopes belong to the harder and stiffer material, i.e. $LiTaO_3$. The detailed view in Fig. 2 represents the initial contact regions of the curves at low loads and low displacements. They show pop-in events in both materials (exemplarily marked by arrows), indicating first deviations from purely elastic contact. These discontinuities occurred at loads of 0.19 ± 0.02 mN and 0.25 ± 0.03 mN at penetration depths of 22.0 ± 2.3 nm and 25.6 ± 2.1 nm for $LiTaO_3$ and $LiNbO_3$, respectively, and were considered as the point where irreversible deformation of the material (e.g. movement of dislocations, twinning, etc.) takes place [39–43].

Table 1 shows the averaged hardness and indentation equivalent elastic moduli values of six Berkovich indents performed for each material, where the latter value was calculated from the obtained reduced modulus during indentation and the materials Poisson's ratio together with elastic constants for the tip which were taken from [44]. The corresponding relationship is thereby described in detail in Section 3.2. It can

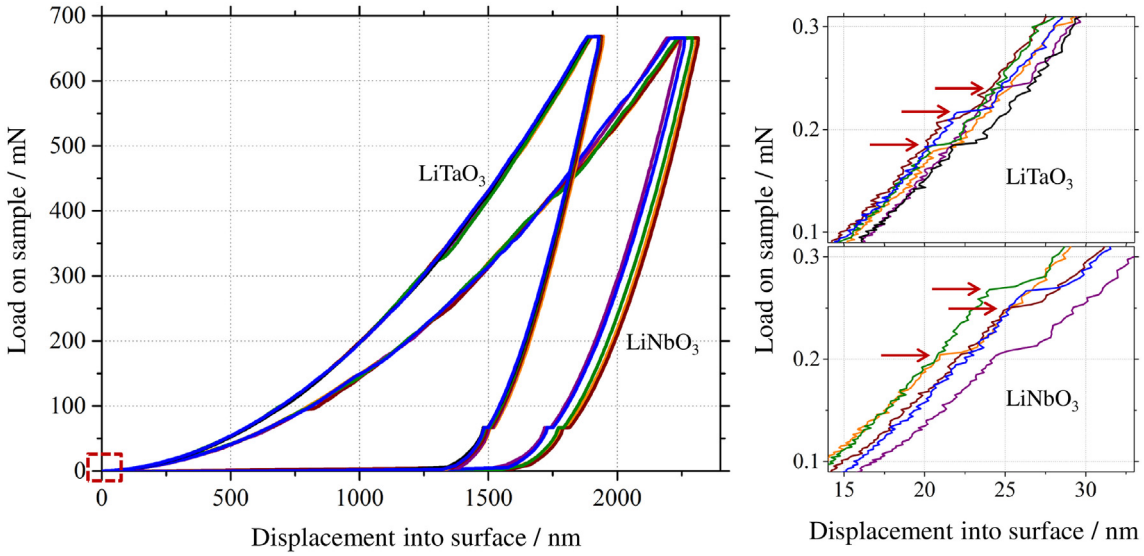

Fig. 2. Load-displacement curves for Berkovich indents into $LiTaO_3$ and $LiNbO_3$ with a detailed view of the first pop-ins (exemplarily highlighted by arrows).

be seen that the hardness of the tested $LiTaO_3$ – with the surface close to $(01\bar{1}2)$ – is almost 50% higher than of the indented $(0\bar{1}14)$ $LiNbO_3$ plane, which is known to be relatively soft [45]. Also the indentation equivalent elastic modulus of $LiTaO_3$ is significantly higher compared to $LiNbO_3$, which was expected comparing the stiffness tensors of both materials [28,29].

During unloading, in particular for brittle materials, cracks may occur due to residual tensile stresses induced from plastic deformation [39,46]. Constant load levels in the unloading curves result from the thermal drift determination at 10% of the maximum load and must not misleadingly be ascribed to any pop-out effects related, for instance, to phase transformations.

Even though Berkovich indentation tests indicate a purely elastic contact prior the first pop-in event, it is advantageous to analyze this effect by spherical nanoindentation. The reason is that using a Berkovich tip is associated with an anisotropic stress and strain field that may influence the mechanical response, as it will promote plastic deformation in certain preferred directions of the anisotropic single crystal. For a general statement on deformation and cracking behavior, several different orientations of the indenter's edges with respect to the crystallographic directions would have to be investigated. Furthermore, the pop-in events occur at relatively low loads (see Fig. 2). This makes it difficult to identify the small residual imprints at this onset of irreversible deformation, and the corresponding analyses of surface and sub-surface damage. Due to the blunted pyramidal tip, which does not necessarily feature a spherical geometry, an analysis of corresponding pop-in stresses is expected to be imprecise. To overcome this challenges spherical nanoindentation tests, which are known to adequately sample effects regarding dislocation densities [47] or crystallographic orientation [48] in single crystals, were performed to apply a more isotropic and less concentrated stress field. The larger activated volume can thereby affect the materials response. Due to the rather low documented dislocation densities of 10^10 m^{-2} and below for $LiTaO_3$ [49] and $LiNbO_3$ [50], respectively, dislocations are expected to be spaced by several μm (assuming a uniform distribution) and may not be activated for the chosen testing configuration. Therefore, homogenous nucleation and correspondingly high stresses close to the theoretical strength may be expected for both materials, even for larger activated volumes using a spherical indenter tip.

Table 1
Indentation equivalent elastic modulus and hardness of $LiTaO_3$ and $LiNbO_3$.

	$LiTaO_3$	$LiNbO_3$
Indentation equivalent elastic modulus [GPa]	248 ± 2	195 ± 1
Hardness [GPa]	9.7 ± 0.1	6.6 ± 0.2

3.2. Material response to spherical nanoindentation tests

Spherical nanoindentation tests were employed using a tip radius of $R = 4.5$ μm. During spherical indentation a symmetrical multiaxial stress field around the indent is introduced, which facilitates the evaluation of damage in the anisotropic materials concerned. The corresponding P–h curves for indentation depths up to ~2 μm are shown in Fig. 3a for $LiTaO_3$ and in Fig. 3b for $LiNbO_3$, respectively. The inserts in Fig. 3 show the detailed pop-in events. It should be noticed that the mean load necessary to induce the pop-ins is slightly higher for $LiNbO_3$ (~75 mN) than for $LiTaO_3$ (~60 mN) and a few orders of magnitude higher than for the Berkovich indentation tests, where higher stress concentrations occur at the sharp tip, in a smaller loaded volume. Furthermore, significant differences in the maximum displacement were measured for each material (see Fig. 3). This can be ascribed to discrete stochastic events occurring in the holding regime at the maximum load, such as the nucleation, propagation and arrest of cracks. However, fractographic results in the next sections could not reveal significant differences in damage morphology associated with such distinct displacement bursts.

Purely elastic Hertzian contact is represented in the figures according to the following equation [51]:

$$P = \frac{4}{3} E^* h^{\frac{3}{2}} \sqrt{R} \tag{1}$$

where P is the load, h is the displacement into the surface, R is the radius of the indenter and E^* is the reduced modulus, which (for isotropic materials) is calculated according to [52]:

$$\frac{1}{E^*} = \frac{1-\nu_s^2}{E_s} + \frac{1-\nu_i^2}{E_i} \tag{2}$$

with E and ν being the Young's modulus and Poisson's ratio of an isotropic sample (s) and the indenter (i), respectively. For anisotropic

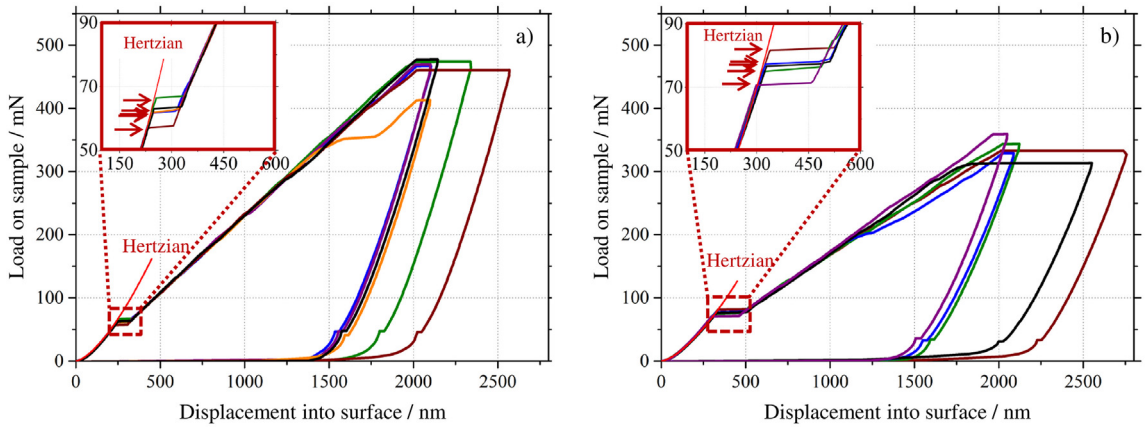

Fig. 3. Load-displacement curves for spherical indents ($R = 4.5$ µm) into a) $LiTaO_3$ and b) $LiNbO_3$. Pop-ins are clearly visible and marked with arrows in the magnified inserts.

materials the theoretical value E^* may also be determined by:

$$\frac{1}{E^*} = \frac{1}{E_{eff}} + \frac{1-\nu_i^2}{E_i} \tag{3}$$

where E_{eff} is the effective indentation modulus that can be calculated based on the elastic constants [33,53,54]. In this work the Hertzian contact P–h relation, as given in Eq. (1), was calculated using E^* from the indentation experiments with $R = 4.5$ µm, $E_i = 1141$ GPa, $\nu_i = 0.07$ and $\nu_s = 0.25$ [44]. The indentation equivalent elastic moduli for both materials were calculated for comparative purposes by transforming Eq. (2) and resulted in $E_{LiTaO3} = 254$ GPa and $E_{LiNbO3} = 195$ GPa, respectively. Both results are in good agreement with the Berkovich indentation results in Table 1.

3.3. Surface damage after spherical indentation

Fig. 4 shows representative surfaces after spherical indents onto $LiTaO_3$ (Fig. 4a, b) and $LiNbO_3$ (Fig. 4d, e) specimens, respectively. Severe damage was observed for all specimens, with cracks always following distinct preferential crystallographic directions. For the $LiTaO_3$ material, cracks were visible along all three $\{01\bar{1}2\}$ planes and also four out of the six $\{11\bar{2}3\}$ planes. The corresponding planes are schematically shown in Fig. 4c (as represented in the corresponding pole figure

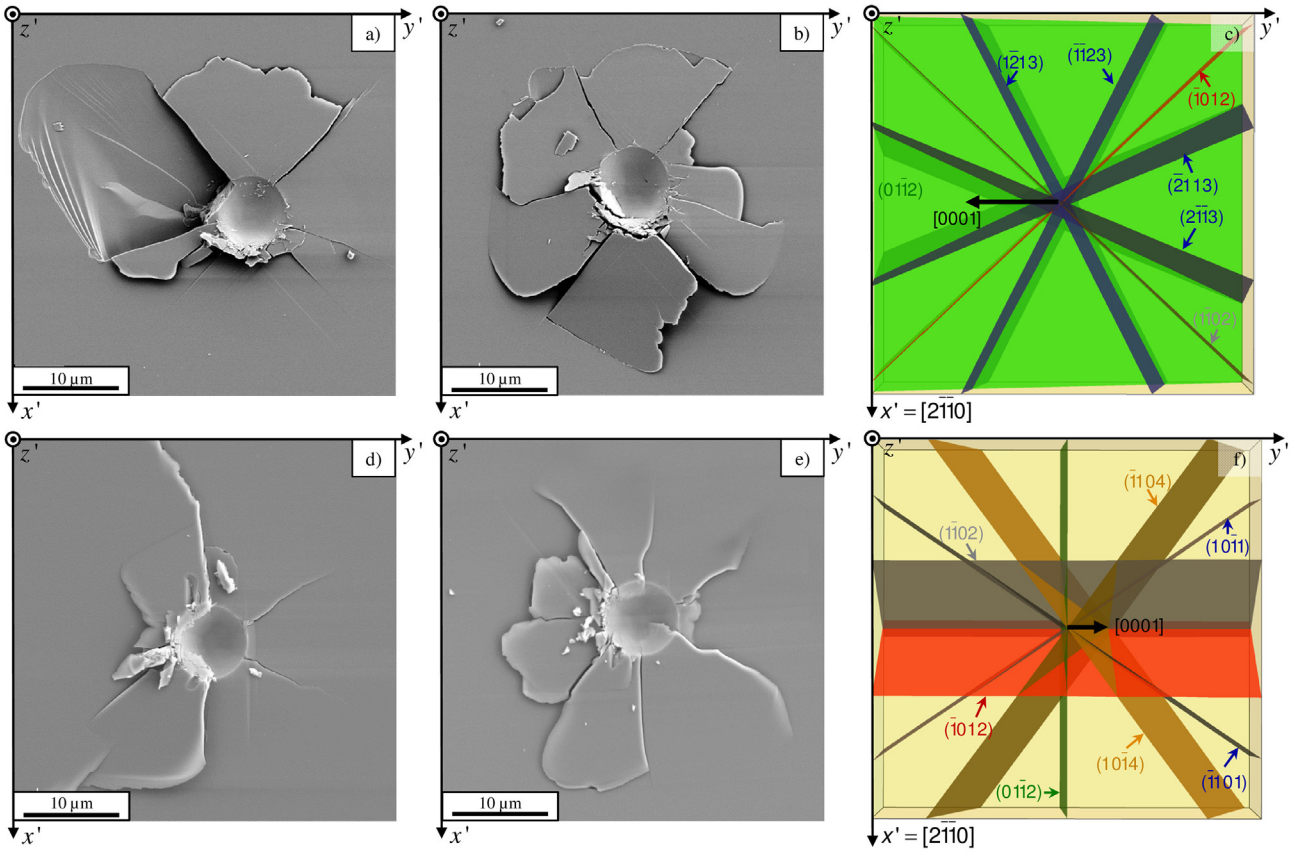

Fig. 4. Representative SEM images after spherical indentation (R = 4.5 µm) with a depth of ~2 µm in $LiTaO_3$ (a, b) and $LiNbO_3$ (d, e). Schematics of frequently activated low indexed planes for $LiTaO_3$ (c) and $LiNbO_3$ (f).

in Fig. 1c). Whereas the activated $(\bar{1}012)$ and $(1\bar{1}02)$ planes both have an angle of 87° with respect to the surface, the $(01\bar{1}2)$ plane is almost parallel (9°) to the surface and is most likely responsible for the chipping of some parts of the material close to the indent. Further cracks, belonging to the $\{11\bar{2}3\}$ set of planes, often occurred along the $(\bar{2}113)$ and $(2\bar{1}\bar{1}3)$ plane, both with an angle of 71° with respect to the surface. Cracks along $(1\bar{2}13)$ and $(\bar{1}\bar{1}23)$ planes, both with an angle of 76° to the surface, were also visible in some specimens. For the two remaining planes belonging to the same family, i.e. $(\bar{1}2\bar{1}3)$ and $(11\bar{2}3)$ with an angle of 27° with respect to the surface, no cracks were observed in any experiment. Also for the $LiNbO_3$ single crystal, severe damage dominated by cracks following preferred crystallographic directions, as those represented in Fig. 4f, was generated in the surface region. Similar to $LiTaO_3$, cracks along the $\{01\bar{1}2\}$ cleavage plane family were always observed. The most pronounced ones were those along the $(01\bar{1}2)$ plane, with an angle of 85° with respect to the surface. Further, slightly smaller cracks along $(\bar{1}101)$ and $(10\bar{1}1)$, both with an inclination angle of 87°, were also visible (see Fig. 4d, e). For some specimens additional cracks along $(1\bar{1}04)$ and $(10\bar{1}4)$, both with an angle of 64° to the surface, could be discerned (compare Fig. 4e, f). Generally, the fracture patterns are similar to those observed for biaxial strength measurements, where also cracks along $\{01\bar{1}2\}$ and $\{11\bar{2}3\}$ for $LiTaO_3$ as well as $\{01\bar{1}2\}$ and $\{10\bar{1}1\}$ for $LiNbO_3$ were documented [18]. Especially the $\{01\bar{1}2\}$ planes are often reported as preferred cleavage planes for this kind of materials [18,26,55]. Cracks along $\{10\bar{1}4\}$ in $LiNbO_3$ have only been reported in this work for the first time.

3.4. Evolution of sub-surface damage

Fig. 5a shows the load-displacement curves of spherical indents with a depth of ~125 nm performed into $LiTaO_3$. Up to this load no pop-ins occurred and, as expected, no plastic deformation was observable on the surface of the specimens after unloading. Further measurements were performed just to the load where the first pop-ins occurred (see Fig. 5b) to examine the surface and sub-surface damages, by setting the displacement limit at a value which is within the expected displacement excursion. The first pop-in events were detected at loads of ~50–55 mN.

Fig. 6a shows a representative surface of a $LiTaO_3$ specimen after this very first contact damage corresponding to one of the load-displacement curves in Fig. 5b. Traces of plastic deformation along the $(\bar{1}012)$ and $(1\bar{1}02)$ planes (shown schematically in Fig. 4c) are visible. In addition to the initial plastic response of the $LiTaO_3$ material, the first cracks can be seen along the same planes. It should be noted that direct observation of the crack onset was not feasible during indentation. All examinations were performed after unloading of the sample. Thus, crack formation might have occurred during the unloading process.

The sub-surface damage was assessed through successive cross-sectioning of the site of interest (see black arrows in Fig. 6a) by using FIB milling. Fig. 6b shows the corresponding section perpendicular to the $(1\bar{1}02)$ plane, as represented in Fig. 6a by a white, dashed line and dashed arrows. The insert in Fig. 6b shows schematically the alignment of these activated planes according to the FIB cut to facilitate the correlation between the crystal orientation and the observed sub-surface crack pattern. It can be seen that a main crack almost perpendicular to the surface initiated upon contact loading. This crack followed the $(1\bar{1}02)$ plane, which lies 87° to the surface. Interestingly, also cracks along the plane $(01\bar{1}2)$ could be observed, which extended almost parallel (i.e. 9°) to the surface. These are responsible for causing "lateral chipping", as observed in Fig. 4. From all traces of plastic deformation visible on the specimen's surface (see Fig. 6a: positions of the "steps" are marked with black arrows) only the most pronounced one turned into a crack. This observation demonstrates that the onset of cracking in these materials is located in regions which were plastically deformed (steps in Fig. 6a), and then proceeds along the cleavage planes $(01\bar{1}2)$ or $(1\bar{1}02)$. Cracks following the $(2\bar{1}\bar{1}3)$ and $(\bar{2}113)$ planes (compare Fig. 6a and Fig. 4c) were significantly longer than those along the $\{01\bar{1}2\}$ planes for every single performed indent indicating a low toughness. Even though the remaining spherical impression had a depth of only ~100 nm (Fig. 5b), cracks down to a depth of ~6 μm could be evidenced (Fig. 6b), thus manifesting the brittle character of the material.

Following the same procedure as for $LiTaO_3$, spherical indentations were performed in the $LiNbO_3$ material. Fig. 7a shows the load-displacement curves up to a maximal load of ca. 60 mN, with a penetration depth of ~250 nm. All specimens (including the one with a slight deviation from linear elastic behavior at 63 mN) were examined in the SEM after the test, showing no visible damage on the surface. An explanation for the slight deviation could thereby be a twin that reversed upon unloading or reversible dislocation loops which could already be documented for $LiTaO_3$ [22]. Since the curve returns to the starting point, no permanent deformation is expected or could be detected on the surface. The first pop-in events were detected at higher loads between 60 and 80 mN (see Fig. 7b), i.e. at higher loads compared to the $LiTaO_3$ specimens (see Fig. 5b). Moreover, the pop-ins occurred over a larger load range.

Fig. 8a shows a representative surface of a $LiNbO_3$ specimen after loading up to the first pop-in shown in Fig. 7b. Analogue to $LiTaO_3$, traces of plastic deformation along the $\{01\bar{1}2\}$ set of planes, which are

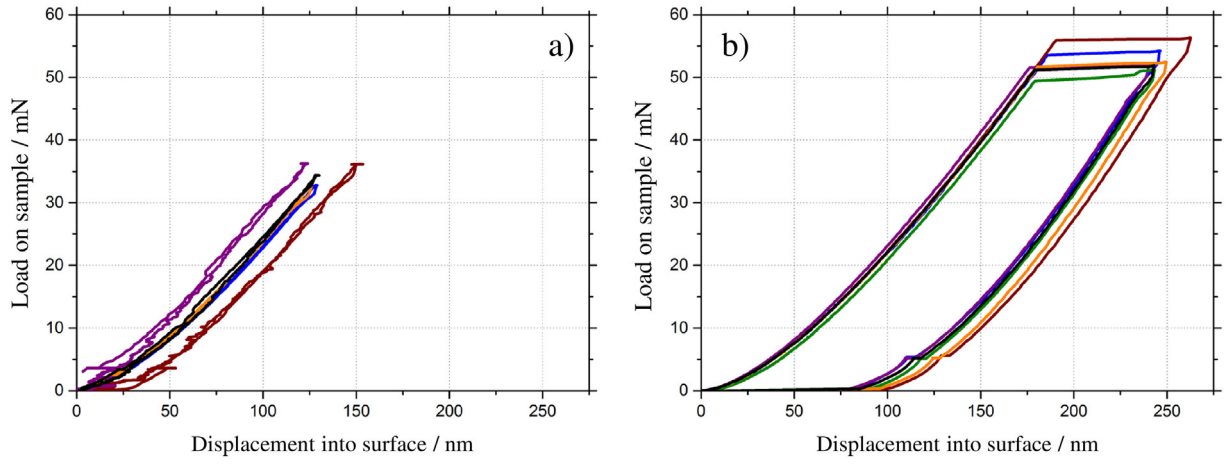

Fig. 5. Load-displacement curves for spherical indents (R = 4.5 μm) in $LiTaO_3$ up to a depth of a) ~125 nm, where no pop-ins were observed and b) where loading was stopped after the first pop-in.

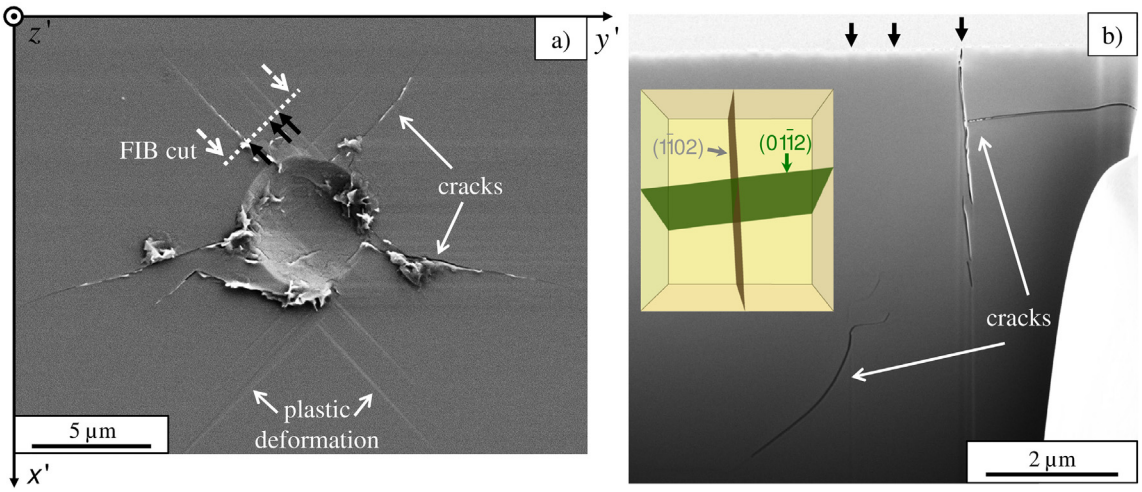

Fig. 6. SEM-image of the surface of a $LiTaO_3$ specimen after spherical indentation (R = 4.5 µm) up to the first pop-in load (a) and FIB cross-section according to the dashed white line in (a) with inserted alignment of the activated {01$\bar{1}$2} cleavage planes (b). Positions of traces of plastic deformation are highlighted with black arrows in both images.

schematically shown in Fig. 4c, are visible. Already after this initial irreversible deformation of $LiNbO_3$, the first cracks are visible along the (01$\bar{1}$2) plane, with an angle of 85° with respect to the surface. The FIB cut perpendicular to the (2$\bar{1}\bar{1}$0) plane provided in Fig. 8b (projection of the cut plane and view direction indicated by white, dashed line and arrows) shows that the sub-surface crack initially follows the (01$\bar{1}$2) plane (see insert in Fig. 8b). However, the penetrating crack also bends into other directions, which cannot be clearly assigned to low-indexed crystallographic planes. Traces of plastic deformation on the specimen's surface were again not possible to be discerned in the cross-sections. The depth of the crack exposed with FIB (Fig. 8b) was about 2 µm, i.e. not as deep as the crack observed in $LiTaO_3$, being in agreement with the shorter cracks visible on the $LiNbO_3$ surfaces. This may be related to the higher elastic modulus of $LiTaO_3$; as the deformation upon loading induces higher stresses under the same applied strain.

3.5. Twinning and cracking

Based upon the experimental observations using spherical indents there seems to be a relation between plastic deformation and cracking in both $LiTaO_3$ and $LiNbO_3$. In this regard, twinning of the {01$\bar{1}$2} planes has been reported for $LiTaO_3$ [22] as well as for $LiNbO_3$ [21,23]. Even at elevated temperatures twinning of the {01$\bar{1}$2} set of planes is still preferred over dislocation glide in $LiTaO_3$ [49] as well as for $LiNbO_3$ [19], providing an explanation for the origin of the observed plastic deformation of $LiTaO_3$ for loading along the c-axis [49]. In our investigation, the traces on the surface of $LiTaO_3$ (Fig. 6a) and on $LiNbO_3$ (Fig. 8a) are aligned along this set of planes (compare with 4c and 4f). Therefore, it can be concluded that for the loading conditions investigated in this work, twinning of the {01$\bar{1}$2} planes is observed. The regarded twinning system with $K_1 = (01\bar{1}2)$, $\eta_1 = [0\bar{1}11]$, $K_2 = (0\bar{1}14)$ and $\eta_2 = [02\bar{2}1]$, as summarized in [56], is shown in Fig. 9 for a cut perpendicular to [2$\bar{1}\bar{1}$0], analogue to the SEM image in Fig. 8b. The small burgers vector of the required partial dislocation of 1/21[01$\bar{1}\bar{1}$] would make this deformation favorable over nucleation of a full dislocation, where the corresponding burgers vector is 1/3[01$\bar{1}\bar{1}$]. The head to head and tail to tail configuration of the polar c-axis caused by twinning leads to charges on these planes which would cause repulsive forces acting on the {01$\bar{1}$2} planes.

To evaluate whether movement of an already existing dislocation might have occurred, an estimation of the corresponding stresses (σ) and flow stresses (τ) out of Berkovich hardness values (H) was performed. For the sake of simplicity, a fully plastic condition (due to the several percent strain occurring in the hardness experiments) and a

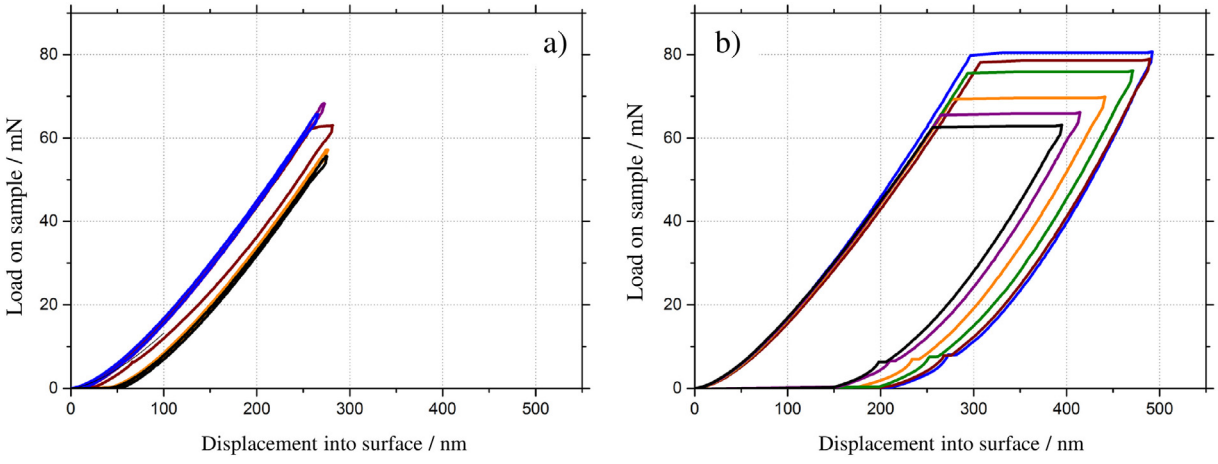

Fig. 7. Load-displacement curves for spherical indents (R = 4.5 µm) in LiNbO3 a) up to a maximal load of ca. 60 mN (with a penetration depth of ~250 nm), where no pop-ins were observed and b) up to 80 mN, where loading was stopped after the first pop-in.

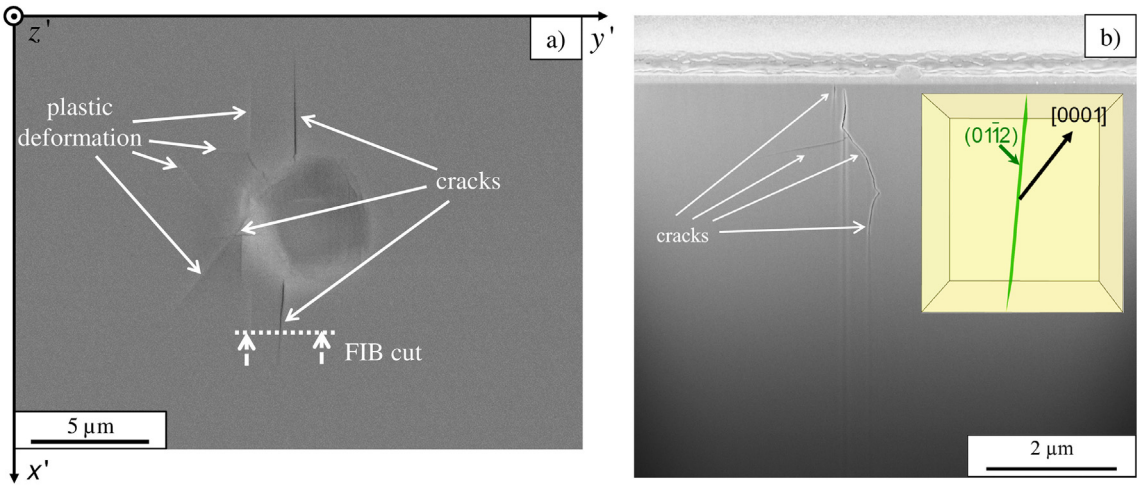

Fig. 8. a) SEM image of the surface of a $LiNbO_3$ specimen after spherical indentation (R = 4.5 µm) up to the first pop-in load and b) FIB cross-section according to the white, dashed line in a) with inserted alignment of the activated (01$\bar{1}$2) cleavage plane.

Tabor's factor of √3 were assumed, leading to the following relationship [57]:

$$\tau = \sigma/\sqrt{3} \quad \text{with} \quad \sigma = H/3 \tag{4}$$

Correspondingly, for the movement of an already existing dislocation, a shear stress of 1.9 GPa for $LiTaO_3$ and 1.3 GPa for $LiNbO_3$ can be estimated from the hardness values shown in Table 1. Since these stresses are significantly lower than those observed in this work (see Section 3.6), glide of existing dislocations can be excluded as predominant deformation mechanism, even if the glide systems were aligned in a disadvantageous way leading to higher required shear stress values. However, also the twin shown in Fig. 9 for $LiNbO_3$ would not explain the surface mark of the indenter after the pop-in, since no shortening in z′ direction is caused by this deformation (only shear strain). Twinning along the ($\bar{1}$012) and (1$\bar{1}$02) would shift the longer c-axis of the crystal almost parallel to the surface and could therefore cause an elongation in plane and consequently a shortening in z′ direction, providing the space for the residual spherical imprint. Furthermore, a relatively high Schmid factor of 0.34 acting on both the ($\bar{1}$012)[$\bar{1}$01$\bar{1}$] and (1$\bar{1}$02)[1$\bar{1}$0$\bar{1}$] system would promote initial plastic deformation along these two planes over the (01$\bar{1}$2)[01$\bar{1}$ $\bar{1}$] system with a Schmid factor of only 0.09. Therefore, the observed twins along the latter system might be the consequence of the changed stress field due to the initial plastic deformation. For $LiTaO_3$ no favorable twinning system could be evidenced, thus requiring plastic shear by dislocations along unknown directions underneath the imprint to realize the prescribed geometry. This might be responsible for the smaller residual depth after the pop-in (compare Figs. 5b and 7b) and the correlated higher hardness.

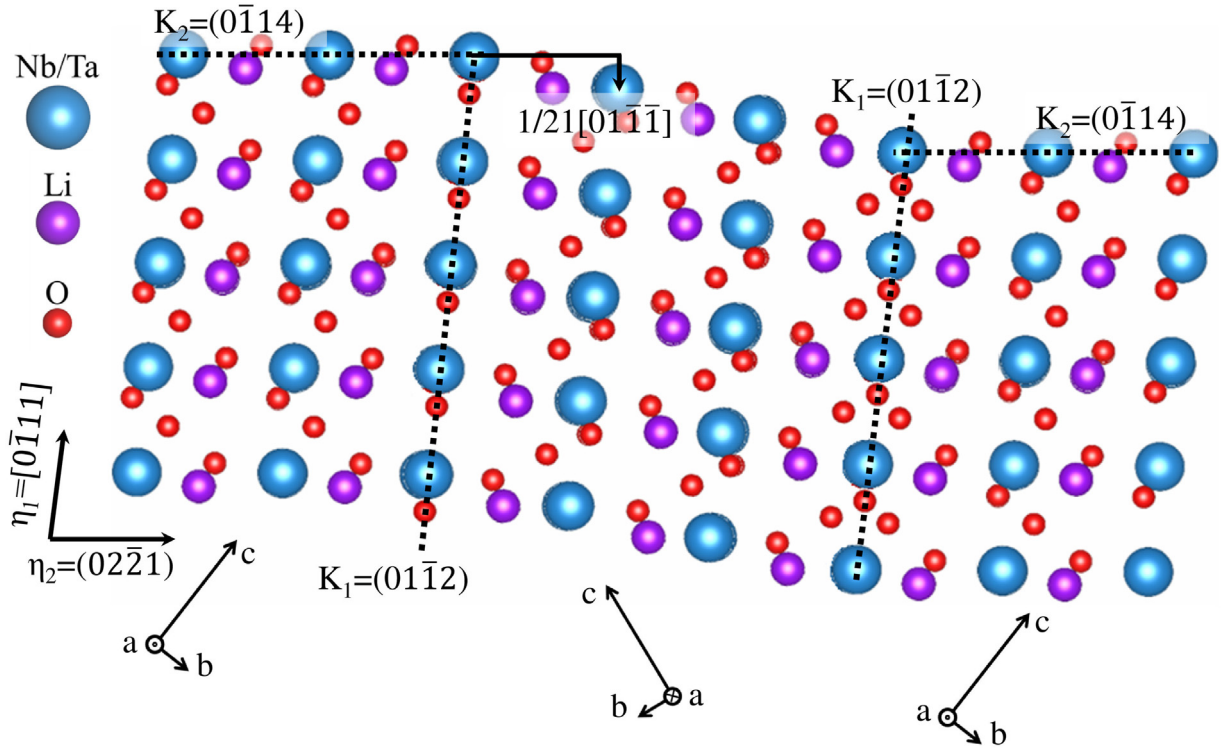

Fig. 9. Schematic representation of a twin domain mirrored onto the (01$\bar{1}$2) plane as observed in $LiNbO_3$ single crystals after spherical indentation.

Also twinning of the {0$\bar{1}$14} planes has previously been reported for $LiTaO_3$ [58], and could be confirmed for $LiNbO_3$ in this work (Fig. 8a). Park et al. [59] documented for $LiNbO_3$ twins as well as cracks along the {01$\bar{1}$2} set of planes and assumed that cracks nucleate at the crossing points of twins. Also in the present work cracks seem to nucleate and propagate at the same planes where twins occurred. Thus it is assumed that these cracks develop due to tensile stresses emerging during unloading and follow the twinned planes, promoted by the repulsive electrostatic forces due to the mirrored alignment of the polar axis. Since this kind of defect is exactly located at documented cleavage planes [18], a significant loss in mechanical strength is expected after the very first pop-in. According to linear elastic fracture mechanics, this effect is expected to be even more severe for $LiTaO_3$, because the cracks penetrate deeper into the material (compare Figs. 6b and 8b). In addition, for larger indents, a gradual increase in damage and thus decrease in mechanical strength may be expected.

3.6. Statistical evaluation of pop-in stresses

In order to rationalize the stresses leading to pop-in events (and eventually cracking) in both materials, a statistical analysis of the pop-in stresses is required. Since the pop-in behavior depends on the activated volume, statistical evaluation of pop-in stresses was performed within the framework of Weibull theory [60]. Weibull parameters were determined by the Maximum-Likelihood method [61] and represented in Weibull plots, where the probability of a pop-in (here considered as a fracture event) is plotted over the maximum shear stress. The maximum occurring shear stresses were evaluated because they might be responsible for the first plastic deformation underneath the indenter. They are significantly higher than those in locations where twin-patterns on the specimen surface were observed. Thus, twinning would be expected as easy deformation mechanism.

Since already the very first pop-in would lower the strength of the investigated single crystal materials due to cracks and twins on the surface, the exact point of this event needs to be evaluated. In total 35 spherical indents were performed for each materials to get significant statistics for the measured pop-in stresses [61]. These stresses were calculated according to Hertzian elastic contact theory, where the maximum shear stress τ_{max} is evaluated by [52]:

$$\tau_{max} = 0.31 \times \left(\frac{6 P_{pop\text{-}in} E^{*2}}{\pi^3 R^2} \right)^{1/3} \quad (5)$$

with $P_{pop\text{-}in}$ being the pop-in load, R the indenter radius and E^* as described in Section 3.2.

In order to prove the suitability of this equation for the anisotropic materials investigated and gain more insight on the stress distribution prior to the pop-in event, a finite element simulation was performed using the commercial software ANSYS 18.2. The materials were treated elastically, namely anisotropic material properties for $LiTaO_3$ and $LiNbO_3$ (as given in [29] at 25 °C) and isotropic elastic constants for the spherical diamond indenter [44]. A contact load corresponding to the average pop-in load (i.e. 79 mN and 57 mN for $LiNbO_3$ and $LiNbO_3$ respectively, see Table 2) was applied within a frictionless contact model. For illustrative purposes, only the numerical results for $LiNbO_3$ are presented in Fig. 10. The referred figure shows a) σ_{Mises}, b) $\sigma_{z'}$, c) σ_{radial}, d) $\sigma_{tangential}$, in $LiNbO_3$, neglecting piezoelectric effects (note: 2nd order mechanical brick elements – SOLID186 - were used). It is worth pointing out that the stresses are not symmetrical with respect to the z′-axis, which is a consequence of the anisotropic elastic constants of the material. The (nearly) circular contact area in $LiNbO_3$ at 79 mN has a radius of 1.22 μm and an in-depth surface displacement of 252 nm, which is consistent with the load-displacement curve in Fig. 7b. The maximum shear stress of 8925 MPa (half of the maximum of σ_{Mises}) is also in good agreement with the approximated experimental shear stress value of 9065 MPa as derived from Eq. (5). For 42° Y-X $LiTaO_3$ the numerical contact analysis for a contact force of 57 mN delivered a contact radius of 1.05 μm, a surface displacement of about 170 nm (cf. Fig. 5b) and a maximum shear stress of 9743 MPa; a value slightly above the experimental result of 9346 MPa (as calculated from Eq. (5)). The resulting stress profiles were similar to those in $LiNbO_3$. However, all stress components (i.e. σ_{Mises}, $\sigma_{z'}$, σ_{radial}, $\sigma_{tangential}$) were slightly higher in $LiTaO_3$ than in $LiNbO_3$, due to the stiffer behavior of the former material. We caution the reader that the incorporation of piezoelectric constants in the model revealed no significant differences concerning Mises stresses, but larger differences for the radial and especially tangential components, which may be related to the selected electrical boundary conditions. However, this is out of the scope of this work. After reliable flow properties of the materials are evaluated, another subject for prospective work will be the assessment of tensile residual stresses suspected to cause cracks during unloading, once irreversible plastic deformation has occurred.

Fig. 11 shows a Weibull plot, where the probability of a pop-in event is plotted vs. the corresponding maximum shear stress, calculated using Eq. (5). For both materials very similar characteristic pop-in stresses were measured. The average as well as the "characteristic" shear stress, τ_0 and the corresponding Weibull modulus, m (slope in the Weibull diagram) are listed in Table 2 along with their 90% confidence intervals. For both materials a characteristic shear stress of ~9 GPa was determined, which equates ~E/27 for $LiTaO_3$ and ~E/22 for $LiNbO_3$, with E being the modulus determined from the spherical indents. These values are already close to the region of the theoretical strength of ~E/8–E/15 [62], supporting the theory of homogenous nucleation due to low defect densities. The pop-in stress values measured for $LiTaO_3$ are slightly higher and within a narrower range, leading to a two times higher Weibull modulus compared to $LiNbO_3$ (see Table 2). The statistical evaluation of the data reveals that the characteristic pop-in stresses in both materials are indeed slightly different within the 90% confidence intervals. It is conspicuous that, although the higher stress values for both materials are almost identical, in $LiNbO_3$ several pop-ins at relatively low loads are present causing the lower Weibull modulus. Nevertheless, the bearable load before pop-in for the same indenter radius is higher for the $LiNbO_3$ due to the lower reduced modulus (see Eq. (5)). Also the contact radius is larger for this material leading to a larger stressed volume which increases the chance of activating a second defect population. This would lead to the pop-ins at relatively low loads (Fig. 11) which also yield a different Weibull modulus. Nevertheless, the origins of defects leading to the observed pop-ins could not be discerned in this work.

Table 2
Average pop-in loads, $P_{pop\text{-}in}$, average shear stresses, τ, characteristic shear stresses, τ_0, and Weibull modulus, m, together with 90% confidence intervals for $LiTaO_3$ and $LiNbO_3$ single crystals obtained after spherical nanoindentation measurements.

	$P_{pop\text{-}in}$ [mN]	τ [MPa]	τ_0 [MPa]	m
$LiTaO_3$	57 ± 5	9226 ± 252	9346 [9278–9415]	42 [32–51]
$LiNbO_3$	79 ± 16	8807 ± 686	9065 [8933–9200]	21 [16–25]

3.7. Understanding crack extension in $LiTaO_3$ and $LiNbO_3$

There seems to be a sort of paradox between the onset of damage and macroscopic mechanical failure in these two materials. On the one hand $LiTaO_3$ is approx. 50% harder than $LiNbO_3$. A direct implication of this higher hardness might be a higher resistance to deformation, indentation or penetration (e.g. due to grinding, impact or wear). As a consequence, smaller defects (e.g. micro-cracks) are expected to be encountered at or below the surface of $LiTaO_3$ samples. The biaxial strength measured in previous work agrees with this hypothesis, where the strength of $LiTaO_3$ was found to be ~2.5 times higher than that of $LiNbO_3$. On the other hand, cross-sectional FIB analysis of the

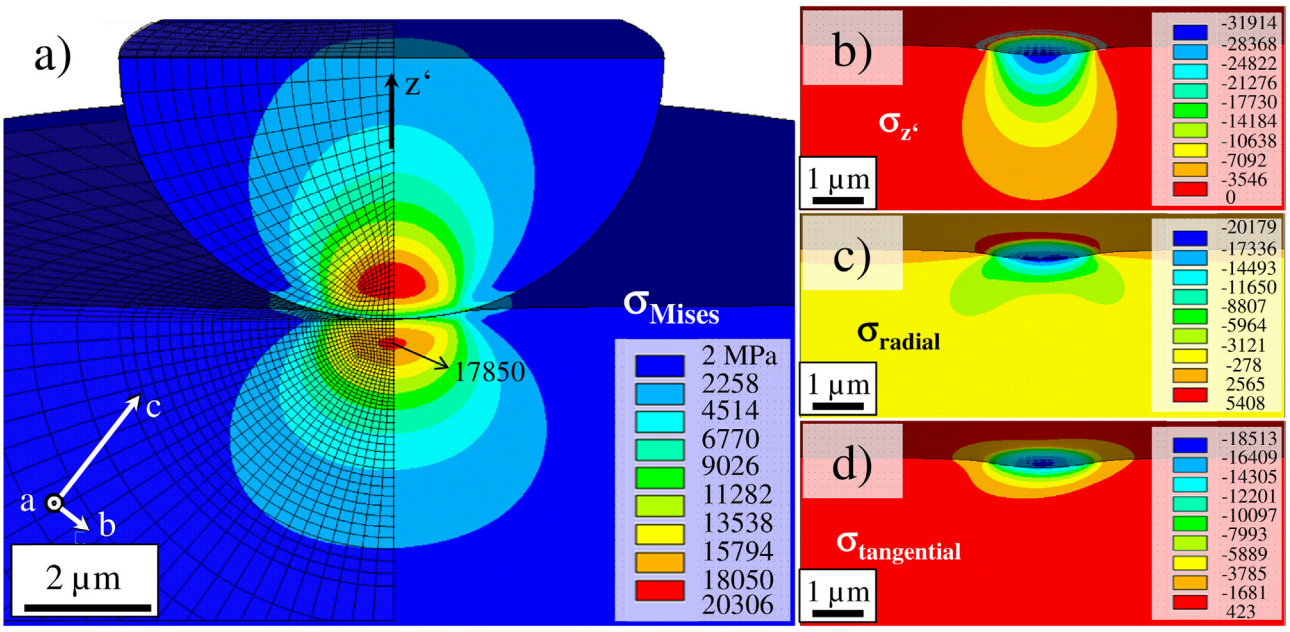

Fig. 10. Contour plots from the elastic frictionless contact analysis showing a) σ_{Mises}, b) $\sigma_{z'}$, c) σ_{radial} and d) $\sigma_{tangential}$ for 128° Y-X $LiNbO_3$ calculated using the commercial finite element software ANSYS 18.2. The stresses are not symmetrical with respect to the z′-axis as a consequence of the anisotropic elastic constants of the material (note: the mesh used for the analysis is shown as an overlay in Fig. 10a, the smallest elements in the contact region have element lengths of about 50 nm).

$LiTaO_3$ and $LiNbO_3$ samples after nanoindentation showed longer extension of the sub-surface cracks in the $LiTaO_3$ samples. The explanation for this may be related to the stored elastic energy during the loading process, which may be different in both materials, and that can trigger the propagation of the originated cracks. According to Ashby [62], the stored elastic energy up to the crack formation can be described as $U_e = \sigma_y^2/2E$ (per volume unit), with σ_y being the yield strength and E the Young's modulus. Approximating the yield strength for both materials to 1/3 of their hardness values [62], and introducing the corresponding indentation equivalent elastic moduli, the stored energy in $LiTaO_3$ is approx. 1.8 times higher than that stored in $LiNbO_3$ [18]. This excess of energy

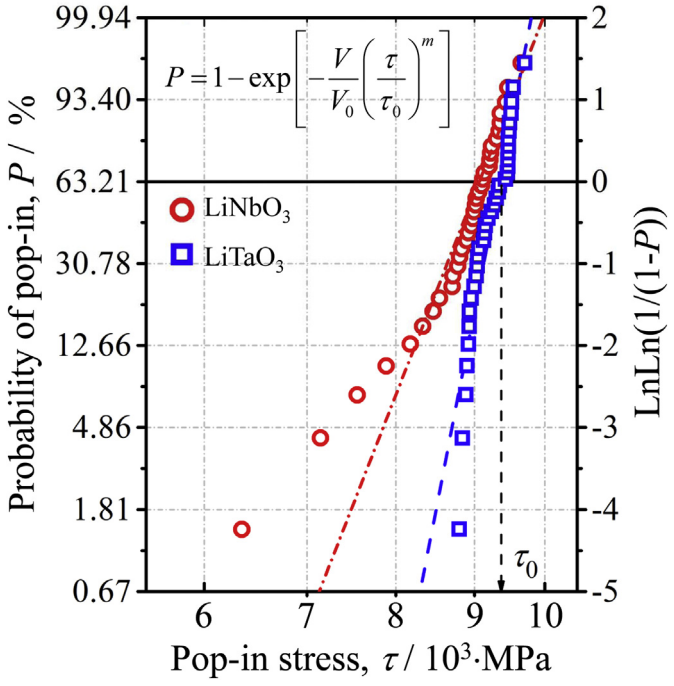

Fig. 11. Weibull diagram showing the probability of pop-in event versus the measured (pop-in) shear stresses for spherical indents (R = 4.5 µm) in $LiTaO_3$ and $LiNbO_3$.

may foster further crack propagation or activation of other cracks in neighboring planes. Even though the introduced damage in $LiTaO_3$ is more severe compared to its $LiNbO_3$ counterpart, it can be concluded that both materials behave similarly with cracks and plastic deformation following certain crystallographic directions. The main difference in the morphology of deformations and cracks can be attributed to the different orientation of the single crystalline materials with respect to the loading direction.

Based upon these findings, the mechanical behavior of single crystals is not only related to the orientation of cleavage planes with respect to the loading direction, but very importantly depends on the type of loading and elastic properties of the material together with its intrinsic toughness, which again varies for different planes. A competition between hardness, toughness, crystal orientation and elastic properties seems to apply. Last but not least, the resistance of the material to the propagation of an existing crack can also play an important role in the macroscopic mechanical behavior of the single crystal. Therefore, fracture toughness measurement in specific cleavage planes is ongoing work.

4. Conclusion

The onset of contact damage in single crystal brittle materials has been investigated on $LiTaO_3$ and $LiNbO_3$ samples combining Berkovich and spherical nanoindentation with FIB sub-surface analyses in the corresponding damaged regions. The materials of study exhibited different contact responses (i.e. crack orientation and length) associated with their distinct intrinsic elastic properties and orientation of brittle cleavage planes with respect to the loading. The onset of contact damage occurs under similar maximum shear stresses in both materials, and is preceded by traces of plastic deformation (twinning) on the contact surface, developed along distinct cleavage planes. These initial locations of plasticity are subsequent sites for crack initiation along those planes. The more pronounced damage in terms of crack length encountered in the $LiTaO_3$ material is ascribed to its higher elastic modulus, and less capability of accommodating plastic deformation. It can be concluded that in anisotropic brittle single crystals the fracture response is determined by a competition between hardness, crystal orientation and elastic properties, and thus must be adequately considered for the design of reliable functional components.

Acknowledgements

Financial support by the Austrian Federal Government (in particular from Bundesministerium für Verkehr, Innovation und Technologie and Bundesministerium für Wissenschaft, Forschung und Wirtschaft) represented by Österreichische Forschungsförderungsgesellschaft mbH and the Styrian and the Tyrolean Provincial Government, represented by Steirische Wirtschaftsförderungsgesellschaft mbH and Standortagentur Tirol, within the framework of the COMET Funding Programme is gratefully acknowledged.

References

[1] C. Campbell, Surface Acoustic Wave Devices and Their Signal Processing Applications, Academic Press, 1989 427–458.
[2] Y.S. Kuz'minov, Lithium Niobate Crystals: Physico-chemical Aspects of Technology, Cambridge International Science Publishing, 1999.
[3] K.-Y. Hashimoto, Surface Acoustic Wave Devices in Telecommunications: Modelling and Simulation, Springer-Verlag Berlin Heidelberg GmbH, 2000.
[4] D. Morgan, Surface Acoustic Wave Filters, 2nd ed. Academic Press, 2007.
[5] Y. Chen, C. Miao, S. Xie, L. Xu, Q. Wang, J. Zhu, et al., Microstructural evolutions, elastic properties and mechanical behaviors of W/Cr Co-doped $Bi_4Ti_3O_{12}$ ceramics, Mater. Des. 90 (2016) 628–634.
[6] S. Jo, C.H. Hong, D.S. Kim, H.W. Kang, C.W. Ahn, H.G. Lee, et al., Phase transition behavior and mechanical properties of (1-x)($Bi_{1/2}Na_{1/2}$)TiO_3-x$SrTiO_3$ lead-free piezoelectric ceramics, Sensors Actuators A Phys. 258 (2017) 201–207.
[7] M. Choi, G. Murillo, S. Hwang, J.W. Kim, J.H. Jung, C.Y. Chen, et al., Mechanical and electrical characterization of PVDF-ZnO hybrid structure for application to nanogenerator, Nano Energy 33 (2017) 462–468.
[8] R.A. Schultz, M.C. Jensen, R.C. Bradt, Single crystal cleavage of brittle materials, Int. J. Fract. 65 (1994) 291–312.
[9] Y.L. Tsai, J.J. Mecholsky Jr, Fracture mechanics description of fracture mirror formation in single crystals, Int. J. Fract. 57 (1992) 167–182.
[10] K.-S. Chen, A. Ayon, S.M. Spearing, Controlling and testing the fracture strength of silicon on the mesoscale, J. Am. Ceram. Soc. 83 (2000) 1476–1484.
[11] A.A. Wereszczak, A.S. Barnes, K. Breder, S. Binapal, Probabilistic strength of {111} n-type silicon, J. Mater. Sci. 11 (2000) 291–303.
[12] C. Funke EK, M. Kuna, H.J. Möller, Biaxial fracture test of silicon wafers, Adv. Eng. Mater. 6 (2004) 594–598.
[13] B.R. Lawn, Indentation of ceramics with spheres: a century after hertz, J. Am. Ceram. Soc. 81 (1998) 1977–1994.
[14] S.K. Lee, B.R. Lawn, Role of microstructure in Hertzian contact damage in silicon nitride: II, strength degradation, J. Am. Ceram. Soc. 81 (1998) 997–1003.
[15] B.R. Lawn, S. Wuttiphan, Model of strength degradation from Hertzian contact damage in tough ceramics, J. Am. Ceram. Soc. 81 (1998) 1509–1520.
[16] Y.-W. Rhee, H.-W. Kim, Y. Deng, B.R. Lawn, Brittle fracture versus quasi plasticity in ceramics: a simple predictive index, J. Am. Ceram. Soc. 84 (2001) 561–565.
[17] M. Deluca, R. Bermejo, M. Pletz, P. Supancic, R. Danzer, Strength and fracture analysis of silicon-based components for embedding, J. Eur. Ceram. Soc. 31 (2011) 549–558.
[18] M. Gruber, I. Kraleva, P. Supancic, J. Bielen, D. Kiener, R. Bermejo, Strength distribution and fracture analyses of $LiNbO_3$ and $LiTaO_3$ single crystals under biaxial loading, J. Eur. Ceram. Soc. 37 (2017) 4397–4406.
[19] A.W. Vere, Mechanical twinning and crack nucleation in lithium niobate, J. Mater. Sci. 3 (1968) 617–621.
[20] K.G. Subhadra, K. Kishan Rao, D.B. Sirdeshmukh, Systematic hardness studies on lithium niobate crystals, Bull. Mater. Sci. 23 (2000) 147–150.
[21] S. Basu, A. Zhou, M. Barsoum, Reversible dislocation motion under contact loading in $LiNbO_3$ single crystal, J. Mater. Res. 23 (2008) 1334–1338.
[22] B. Anasori, K.E. Sickafus, I.O. Usov, M.W. Barsoum, Spherical nanoindentation study of the deformation micromechanisms of $LiTaO_3$ single crystals, J. Appl. Phys. 110 (2011), 023516. .
[23] Z. Zhang, S. Yang, C. Xu, B. Wang, N. Duan, Deformation and stress at pop-in of lithium niobate induced by nanoindentation, Scr. Mater. 77 (2014) 56–59.
[24] K. Shibayama, K. Yamanouchi, H. Sato, T. Meguro, Optimum cut for RoV-Cut $LiNb0_3$ crystal used as the substrate of acoustic-surface-wave filters, Proc. IEEE 64 (1976) 595–597.
[25] W. Weng, H. Wang, N. Ma, Y. Wu, J. Li, Effect of domain structure on the damping properties of $LiNbO_3$/Al composites, Mater. Des. 31 (2010) 4116–4121.
[26] R.S. Weis, T.K. Gaylord, Lithium niobate: summary of physical properties and crystal structure, Appl. Phys. A Mater. Sci. Process. 37 (1985) 191–203.
[27] S.C. Abrahams, J.M. Reddy, J.L. Bernstein, Ferroelectric lithium niobate. 3. Single crystal X-ray diffraction study at 24 °C, J. Phys. Chem. Solids 27 (1966) 997–1012.
[28] K. Taki, Y. Shimizu, Material constants of $LiTaO_3$ determined from surface acoustic wave velocities, Jpn. J. Appl. Phys. 33 (1994) 2976–2978.
[29] R.T. Smith, F.S. Welsh, Temperature dependence of the elastic, piezoelectric, and dielectric constants of lithium tantalate and lithium niobate, J. Appl. Phys. 42 (1971) 2219–2230.
[30] R. Hsu, E.N. Maslen, D. Du Boulay, N. Ishizawa, Synchroton X-ray studies of $LiNbO_3$ and $LiTaO_3$, Acta Crystallogr. B 53 (1997) 420–428.
[31] B. Merle, V. Maier-Kiener, G.M. Pharr, Influence of modulus-to-hardness ratio and harmonic parameters on continuous stiffness measurement during nanoindentation, Acta Mater. 134 (2017) 167–176.
[32] W.C. Oliver, G.M. Pharr, An improved technique for determining hardness and elastic modulus using load and displacement sensing indentation experiments, J. Mater. Res. 7 (1992) 1564–1583.
[33] J.J. Vlassak, W.D. Nix, Indentation modulus of elastically anisotropic half spaces, Philos. Mag. A 67 (1993) 1045–1056.
[34] J.J. Vlassak, W.D. Nix, Measuring the elastic properties of anisotropic materials by means of indentation experiments, J. Mech. Phys. Solids 42 (1994) 1223–1245.
[35] A. Leitner, V. Maier-Kiener, D. Kiener, Essential refinements of spherical nanoindentation protocols for the reliable determination of mechanical flow curves, Mater. Des. 146 (2018) 69–80.
[36] T. Zhu, J. Li, A. Samanta, A. Leach, K. Gall, Temperature and strain-rate dependence of surface dislocation nucleation, Phys. Rev. Lett. 100 (2008), 025502. .
[37] S. Shim, H. Bei, E.P. George, G.M. Pharr, A different type of indentation size effect, Scr. Mater. 59 (2008) 1095–1098.
[38] Y. Gao, H. Bei, Strength statistics of single crystals and metallic glasses under small stressed volumes, Prog. Mater. Sci. 82 (2016) 118–150.
[39] B.R. Lawn, A.G. Evans, D.B. Marshall, Elastic/plastic indentation damage in ceramics: the median/radial crack system, J. Am. Ceram. Soc. 63 (1980) 574–581.
[40] C.A. Schuh, J.K. Mason, A.C. Lund, Quantitative insight into dislocation nucleation from high-temperature nanoindentation experiments, Nat. Mater. 4 (2005) 617–621.
[41] Y. Gaillard, A.H. Macías, J. Muñoz-Saldaña, M. Anglada, G. Trápaga, Nanoindentation of $BaTiO_3$: dislocation nucleation and mechanical twinning, J. Phys. D 42 (2009), 085502. .
[42] W.W. Gerberich, S.K. Venkataraman, H. Huang, S.E. Harvey, D.L. Kohlstedt, The injection of plasticity by millinewton contacts, Acta Metall. Mater. 43 (1995) 1569–1576.
[43] R.J. Asaro, S. Suresh, Mechanistic models for the activation volume and rate sensitivity in metals with nanocrystalline grains and nano-scale twins, Acta Mater. 53 (2005) 3369–3382.
[44] G. Simmons, H. Wang, Single Crystal Elastic Constants and Calculated Aggregate Properties: A Handbook, 2nd ed. MIT Press, Cambridge, MA, 1971.
[45] S. Bhagavat, I. Kao, Nanoindentation of lithium niobate: hardness anisotropy and pop-in phenomenon, Mater. Sci. Eng. A 393 (2005) 327–331.
[46] M. Sebastiani, K.E. Johanns, E.G. Herbert, G.M. Pharr, Measurement of fracture toughness by nanoindentation methods: recent advances and future challenges, Curr. Opin. Solid State Mater. Sci. 19 (2015) 324–333.
[47] Z. Wang, H. Bei, E.P. George, G.M. Pharr, Influences of surface preparation on nanoindentation pop-in in single-crystal Mo, Scr. Mater. 65 (2011) 469–472.
[48] O. Franke, J. Alcalá, R. Dalmau, Z.C. Duan, J. Biener, M. Biener, et al., Incipient plasticity of single-crystal tantalum as a function of temperature and orientation, Philos. Mag. 95 (2015) 1866–1877.
[49] P. Cordier, B. Boulogne, N. Dotikiian, J. Doukhan, Lattice defects in lithium tantalate, Phys. Status Solidi A 112 (1989) 493–510.
[50] K. Sugh, H. Iwasaki, S. Miyazawa, N. Nuzeki, An x-ray topographic study on lithium niobate single crystals, J. Cryst. Growth 18 (1973) 159–166.
[51] B.R. Lawn, Fracture of Brittle Solids, Second edition Cambridge University Press, Cambridge, 1993.
[52] K.L. Johnson, Contact Mechanics, Cambridge University Press, Cambridge, 1985.
[53] J.R. Willis, Hertzian contact of anisotropic bodies, J. Mech. Phys. Solids 14 (1966) 163–176.
[54] J.G. Swadener, G.M. Pharr, Indentation of elastically anisotropic half-spaces by cones and parabolae of revolution, Philos. Mag. A 81 (2001) 447–466.
[55] W. Hang, L. Zhou, J. Shimizu, J. Yuan, T. Yamamoto, Study on the Mechanical Properties of Lithium Tantalate and the Influence on its Machinability, 7, Fuji Technology Press LTD, 2013 644–653.
[56] K.K. Wong, Properties of Lithium Niobate: INSPEC, The Institution of Electrical Engineers, London, United Kingdom, 2002.
[57] W.D. Nix, H. Gao, Indentation size effects in crystalline materials: a law for strain gradient plasticity, J. Mech. Phys. Solids 46 (1998) 411–425.
[58] L.A. Bursill, P.J. Lin, Chemical twinning and ferroelectric domains in $LiTaO_3$, Philos. Mag. A 46 (1982) 1–24.
[59] B.M. Park, K. Kitamura, Y. Furukawa, Y. Ji, Relation between mechanical twinning and cracking in stoichiometric lithium niobate single crystals, J. Am. Ceram. Soc. 80 (1997) 2689–2692.
[60] W. Weibull, A statistical distribution function of wide applicability, J. Appl. Mech. 18 (1951) 293–297.
[61] EN 843-5, Advanced Technical Ceramics - Monolithic Ceramics - Mechanical Tests at Room Temperature - Part 5: Statistical Analysis, 2006 (EN 843-51997. p. 40).
[62] M.F. Ashby, D.R.H. Jones, Engineering Materials 1, Pergamon Press, Oxford, 1993.